International Journal of Plasticity 172 (2024) 103821

Contents lists available at ScienceDirect

International Journal of Plasticity

journal homepage: www.elsevier.com/locate/ijplas

Improving ductility by coherent nanoprecipitates in medium entropy alloy

Zihan Zhang [a,b], Yan Ma [a,c,*], Muxin Yang [a], Ping Jiang [a], Hangqi Feng [a], Yuntian Zhu [c], Xiaolei Wu [a,b], Fuping Yuan [a,b,*]

[a] State Key Laboratory of Nonlinear Mechanics, Institute of Mechanics, Chinese Academy of Sciences, Beijing 100190, China
[b] School of Engineering Science, University of Chinese Academy of Sciences, Beijing 100049, China
[c] Department of Materials Science and Engineering, City University of Hong Kong, Hong Kong, China

ARTICLE INFO

Keywords:
Medium-entropy alloys
Ductility
Coherent nanoprecipitates
9R structures
Precipitation hardening

ABSTRACT

Controlling precipitates in spatial density and size distribution is essential for tailoring the microstructure and mechanical properties through precipitation hardening. We herein obtained heterogeneous grain structures with coherent $L1_2$ nanoprecipitates in $(CrCoNi)_{94}Al_4Ti_2$ medium entropy alloy (MEA) by annealing and aging. Additional pre-aging leads to a high spatial density and more random distribution nucleation sites of the coherent $L1_2$ nanoprecipitates. The pre-aging doubled the ductility without apparently sacrificing the strength. Transmission electron microscopy (TEM) revealed that, in pre-aged MEA, finely dispersed $L1_2$ nanoprecipitates with higher spatial density were sheared by dislocation, promoting planar slips, which favors geometrically necessary dislocations (GNDs) piling up to increased hetero-deformation-induced (HDI) stress and work-hardening. Stacking faults, Lomer-Cottrell locks, and 9R structures were formed in aged and pre-aged MEA after tensile deformation. The formation of these defects enormously enhanced strain hardening by blocking dislocation movements and accumulating dislocations. Moreover, a higher frequency of interactions between defects and coherent $L1_2$ nanoprecipitates can be observed in the pre-aged MEA due to the more randomly distributed $L1_2$ nanoprecipitates, substantially increasing ductility. This work demonstrates a new route to achieving a super strength-ductility combination of single-phase FCC high entropy alloys by nanoscale coherent precipitation strengthening.

1. Introduction

Single-phase face-centered cubic (FCC) alloys containing multi-principal elements, which are also named high-entropy alloys (HEAs) or medium-entropy alloys (MEAs) (George et al., 2019; Ma and Wu, 2019; Cao et al., 2021; Yeh et al., 2004), have been intensely studied in recent years due to their unique and attractive tensile properties (Jo et al., 2017; Li et al., 2016; Liang et al., 2018) and fracture toughness (Gludovatz et al., 2014, 2016; Yang et al., 2021). The superior mechanical properties in these FCC single-phase M/HEAs have been attributed to not only the traditional mechanisms, such as lattice distortion (Fantin et al., 2020; Sohn et al., 2019) and sluggish diffusion effect (Wang et al., 2019), but also the novel mechanisms, such as unevenly distributed stacking fault energy with atomic level (An et al., 2023; Li et al., 2019; Wagner and Laplanche, 2023) and chemical short/medium-range orders (Chen et al.,

* Corresponding authors.
E-mail addresses: mayan@imech.ac.cn (Y. Ma), fpyuan@lnm.imech.ac.cn (F. Yuan).

https://doi.org/10.1016/j.ijplas.2023.103821
Received 15 August 2023; Received in revised form 9 November 2023;
Available online 22 November 2023

2021b; Seol et al., 2022; Wang et al., 2022; Zhang et al., 2020; Zhou et al., 2022).

The application of single-phase FCC M/HEAs with coarse grains would be limited due to the relative low yield strength. Plastic deformation and aging treatments are usually employed to improve the strength of M/HEAs by dislocation hardening (Wu et al., 2015; Yang et al., 2018a; Zhu and Liao, 2004) and precipitation hardening (Xu et al., 2019; He et al., 2016). Nevertheless, strengthening by nanostructured grains or incoherent precipitates with larger sizes inevitably leads to a dramatic reduction in ductility (Du et al., 2020; Liu et al., 2022; Zhao et al., 2023). However, sometimes, coherent nanoprecipitates can relieve the dilemma of strength-ductility trade-off, producing a superior combination of yield strength and ductility (Fan et al., 2020; Yang et al., 2019, 2018b). The problems of stress/strain concentration in metals with large-size incoherent precipitates can be avoided by coherent nanoprecipitates (Jodi et al., 2019; Yang et al., 2018b). Moreover, fixed volume fractions of nanoprecipitates result in significantly higher spatial precipitate density than micrometer-size precipitates, leading to increased precipitation hardening. Thus, better ductility may be obtained by deploying nanoprecipitates with coherent interfaces (Yang et al., 2018b; Fan et al., 2020).

The strengthening strategy by coherent nanoprecipitates has also been applied to M/HEAs recently (Fan et al., 2020; Jodi et al., 2019; Yang et al., 2019, 2018b). Both high yield strength and high ductility were obtained in many M/HEA systems, such as $(CoCrNi)_{94}Al_3Ti_3$ MEA (Du et al., 2020; Zhang et al., 2022e, 2022c), $Al_{0.5}Cr_{0.9}FeNi_{2.5}V_{0.2}$ HEA (Qin et al., 2022a, 2023; Qin et al., 2022b, 2022c), and $(FeCoNi)_{86}Al_7Ti_7$ MEA (Cheng et al., 2022; Peng et al., 2023; Xu et al., 2023). In metals and alloys with coherent nanoprecipitates, the tensile properties can be optimized by adjusting the dimension, shape, distribution, element concentrations, and interspacing of coherent nanoprecipitates (Xu et al., 2019). Besides substantial precipitation hardening and other deformation mechanisms, such as micro-bands and high density of stacking fault networks, were also found to play crucial roles in the high-performance M/HEAs (Cheng et al., 2022; Fan et al., 2020; Yang et al., 2018b). However, controlling the size of precipitation is a great challenge by adjusting the annealing until peak aging, i.e., prioritizing the shear mechanism of nanoscale precipitating to improve the strength and ductility together (Chen et al., 2021a; Chou et al., 2022).

In this work, we used pre-aging treatment before annealing in $(CoCrNi)_{94}Al_4Ti_2$ MEA to activate multiple strengthening and strain-hardening mechanisms. High spatial and randomly distributed coherent $L1_2$ nanoprecipitates were formed in the heterogeneous structured FCC matrix by adjusting the aging treatment. The obtained MEAs show better ductility with similar yield strength. The corresponding strengthening mechanisms of precipitates are investigated by tensile testing and microstructure characterizations. This work demonstrates a new thermal-processing route to achieve a super strength-ductility combination for single-phase M/HEAs by more randomly distributed nanoscale coherent precipitates along with heterogeneous grain structures.

2. Materials and experimental procedures

The $(CoCrNi)_{94}Al_4Ti_2$ MEA was melted in a vacuum arc furnace, and the actual chemical composition is $Co_{34.46}Cr_{32.12}Ni_{27.42}Al_4Ti_2$ (in at.%). The MEA was re-melted several times under the argon atmosphere to ensure homogeneity for each element and then cast into ingots. The ingots were hot forged into 10 mm thick plates at 1223 K, followed by solution annealing at 1473 K for two hours and then water quenching to obtain a single FCC phase with coarse grains. Finally, these plates were cold rolled (CR) with multiple passes to reduce thickness by about 90 %.

Four different heat-treatment procedures were applied to these CR plates to adjust the size and distribution of precipitates. First, some plates were annealed at 1123, 1173, and 1223 K for one hour and water quenched, named AN1123, AN1173, and AN1223, respectively. Second, some plates were first pre-aged at 973 K for four hours and then annealed at 1123, 1173, and 1223 K for one hour with water quenching, which were referred to as PA-AN1123, PA-AN1173, and PA-AN1223, respectively. Third, some plates were first annealed at 1123, 1173, and 1223 K for one hour, and then aged at 973 K for four hours with water quenching, named AN1123-AG, AN1173-AG, and AN1223-AG, respectively. Fourth, some plates were first pre-aged at 973 K for four hours, then annealed at 1123, 1173, and 1223 K for one hour, and last aged at 973 K again for four hours with water quenching, which were referred to as PA-AN1123-AG, PA-AN1173-AG, and PA-AN1223-AG, respectively. Overall, the low aging temperature was designed to avoid grain coarsening and abnormal grain growth, while the higher annealing temperature could encourage partial recrystallization and grain coarsening, promoting heterogeneous grain structures. The MEAs treated in the second and fourth processes were pre-aged compared to the MEAs treated in the first and third processes. Thus, the effect of the pre-aging treatment on the size and distribution of coherent nanoprecipitates on the tensile behaviors can be revealed.

Tensile specimens were dog-bone shaped and machined by electric discharge machining to a gauge section of 18 mm in length, 2.5 mm in breadth, and 1.0 mm in thickness (based on ISO6892–1998 standard). Tensile tests were conducted on an Instron 5967 testing machine with a strain rate of $5 \times 10^{-4}\ s^{-1}$ at room temperature. An extensometer was used to measure the tensile displacement. The tensile test was repeated three times at least for each heat-treated sample. Energy dispersive spectroscopy (EDS) and X-ray diffraction (XRD) were used to characterize the element distributions and the volume fractions of various phases, respectively. Electron backscattered diffraction (EBSD), transmission electron microscopy (TEM), and high-resolution TEM (HRTEM) were used to characterize the microstructures of samples. The detailed procedures for sample preparation and the other information for EBSD, TEM, and HRTEM observations can be found in our previous papers (Ma et al., 2018; Zhang et al., 2022d).

3. Results and discussion

3.1. Microstructures of MEA

The microstructures of four selected samples (AN1173, PA-AN1173, AN1173-AG, and PA-AN1173-AG) for each heat-treatment

procedure were depicted by EBSD band contrast (BC) figures before tensile testing in Fig. 1. The results show that all samples have heterogeneous grain sizes ranging from 0.11 μm to ~5.0 μm, in which the fine-grain region was separated by a coarse-grain region without a clear boundary (Fig. 1e-f). The corresponding average grain sizes were 1.23 ± 0.66, 1.14 ± 0.68, 0.84 ± 0.56, and 0.78 ± 0.37 μm, respectively. Annealing twins are observed with high density in all samples. The grain sizes of aged samples (AN1173-AG and PA-AN1173-AG) are moderately smaller than those of annealed samples (AN1173 and PA-AN1173). This refinement was controlled by the second recrystallization during aging, in which the formation of grain nuclei and slight grain growth happened at the relatively low aging temperature (Song et al., 2021). Notably, the average grain sizes of pre-aged samples are similar to those without pre-aged procedures. These observations suggest that the effect of the pre-aged procedure is mainly on the size and distribution of the coherent nanoprecipitates, as will be confirmed by the following observations.

The XRD patterns for the four samples mentioned above are given in Fig. 2a. As shown in Fig. 2b-e, the amplified (111) diffraction peaks exhibit an asymmetry due to the overlap of the peaks of the FCC matrix and coherent $L1_2$ phase. The asymmetric peak can be deconvoluted into two separated symmetric peaks for the FCC matrix and $L1_2$ phase by Gauss function fitting. Then, the relative volume fraction of both phases can be estimated by the integrated areas of these two symmetric peaks (Liu et al., 2023a; Ma et al., 2021; Zhang et al., 2022a). The relative volume fractions of the $L1_2$ phase for the four samples were estimated to be about 10.0 %, 13.2 %, 18.2 %, and 20.3 %, respectively. These results indicate that the pre-aging can slightly increase the volume fraction (2.1–3.2 %) of

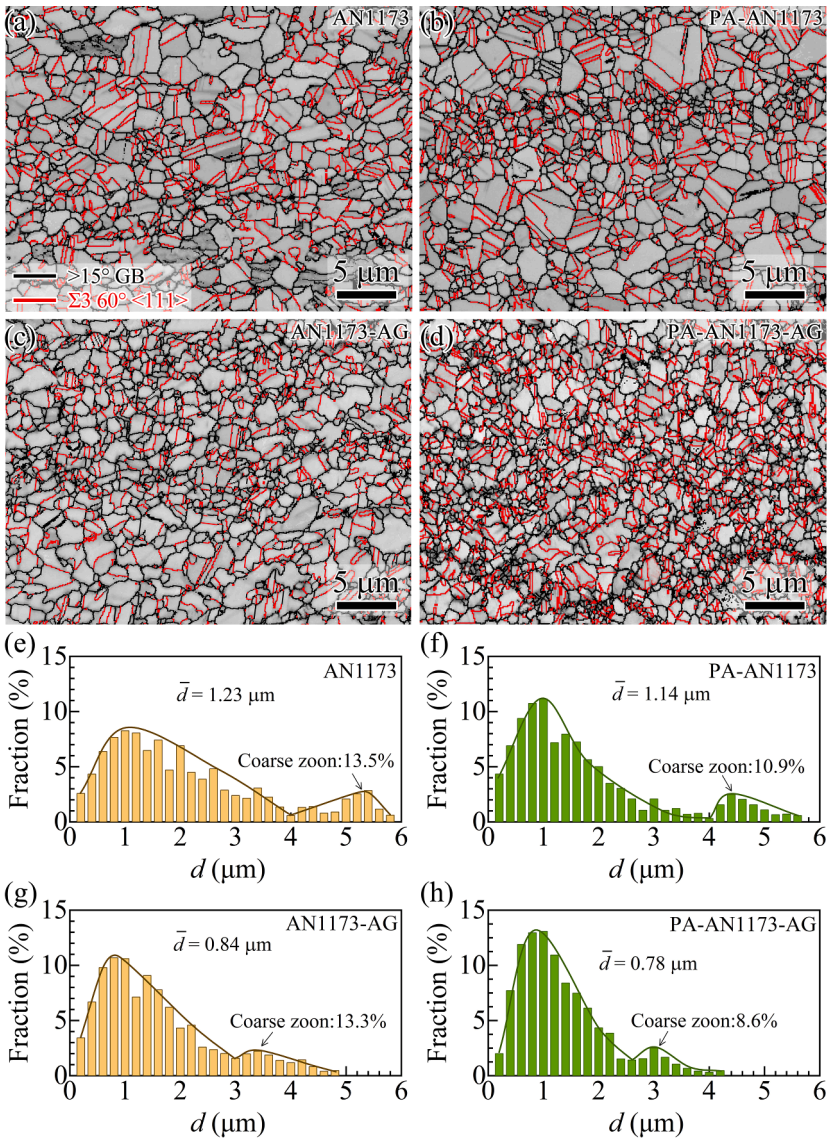

Fig. 1. Microstructures of four typical samples upon each heat treatment by EBSD. Band contrast figures of (a) AN1173, (b) PA-AN1173, (c) AN1173-AG, (d) PA-AN1173-AG. Black lines note grain boundaries, and red lines note twin boundaries. The statistical results of grain size distribution for (e) AN1173, (f) PA-AN1173, (g) AN1173-AG, (h) PA-AN1173-AG.

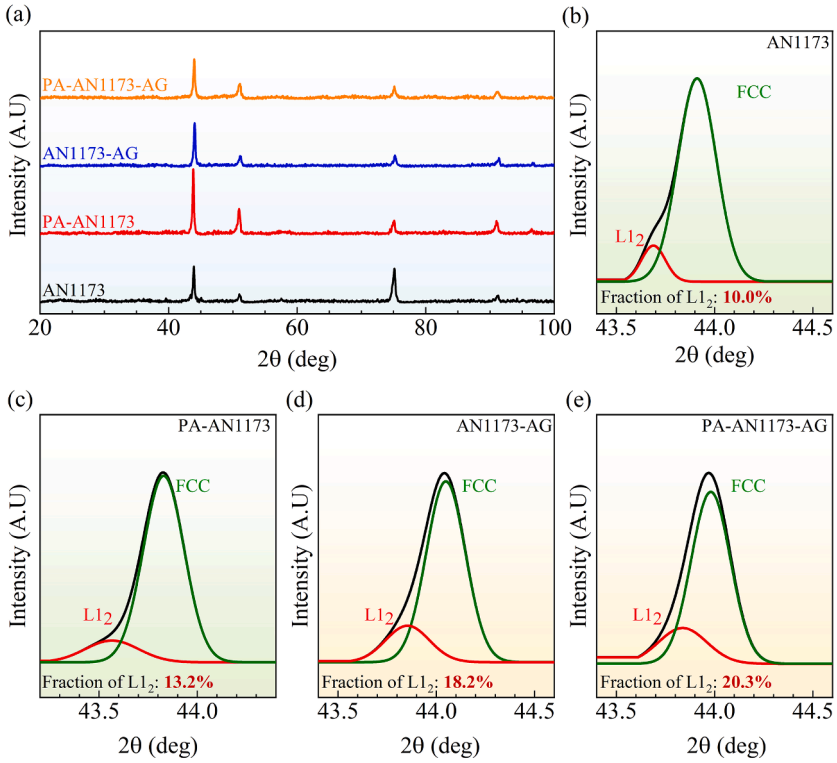

Fig. 2. Phase identification via X-ray diffraction (XRD) analysis. (a) XRD patterns for four typical samples of each heat-treatment procedure (AN1173, PA-AN1173, AN1173-AG, PA-AN1173-AG). The asymmetric (111) diffraction peaks and the deconvoluted symmetric peaks of coherent FCC and $L1_2$ phases for (b) AN1173, (c) PA-AN1173, (d) AN1173-AG, (e) PA-AN1173-AG.

the $L1_2$ phase, while post-aging can significantly increase it (7.1–8.2 %). Accordingly, additional pre-aging can produce high-density nucleation sites of the coherent $L1_2$ nanoprecipitates for the MEA.

TEM and HRTEM images for AN1173 and PA-AN1173 samples are displayed in Fig. 3a-c and Fig. 3d-f, respectively. As shown in Fig. 3a and d, heterogeneous grain structures are observed in both samples. The density of annealing twins in the PA-AN1173 sample (Fig. 3d) is a little higher than that of AN1173 (Fig. 3a), which is consistent with the EBSD results (Fig. 1a and b). The size and distribution of the $L1_2$ phase for these two samples are revealed in Fig. 3b and e. It is noteworthy that the $L1_2$ phase in PA-AN1173 is more randomly distributed, and the number density is much larger than that of AN1173. Selected area electron diffractions (SAED) in the insets of Fig. 3b and e exhibit superlattice reflection, confirming the coherence of FCC and $L1_2$ phases. The apparent difference between PA-AN1173 and AN1173 samples reveals that the pre-aging on the CR sample, in the high-density-defects state, can facilitate precipitating due to the higher stored distortion energy (Du et al., 2020). HRTEM images in Fig. 3c and f show the coherent interfaces of the FCC and $L1_2$ phases. The EDS mapping for an area with several $L1_2$ nanoprecipitates is demonstrated in Fig. 3g, and the element concentrations along the marked line are displayed in Fig. 3h. It reveals the significant enrichment of Ni, Al, and Ti elements in precipitates, Co and Cr elements are depleted in precipitates. The present MEA has the same element diffusion trades as reported previously (Fan et al., 2020; Yang et al., 2018b), which can improve strain hardening by facilitating the dislocation slips.

The corresponding results of AN1173-AG and PA-AN1173-AG by TEM, HRTEM, and EDS mapping are shown in Fig. 4. It is observed that the $L1_2$ nanoprecipitates are not randomly distributed in the AN1173-AG sample, and both large and small sizes of $L1_2$ nanoprecipitates can be found in the AN1173-AG sample (Fig. 4a-b). In contrast, the dimensions of $L1_2$ nanoprecipitates are very similar (~10 nm), and they were randomly distributed in the PA-AN1173-AG sample (Fig. 4d-e). The element concentrations of the $L1_2$ phase of the aged samples are consistent with annealed samples (AN1173 and PA-AN1173), as shown in Fig. 4g and h. Hence, the effects of element and composition in the $L1_2$ nanoprecipitates could be disregarded. Combining the results of Figs. 3 and 4, we can conclude that more uniform sizes and random distribution of $L1_2$ nanoprecipitates can be achieved by pre-aging treatment in the present MEA.

3.2. *Mechanical properties of MEA*

Tensile properties of the MEA subjected to four different heat treatment procedures are compared in Fig. 5. The engineering stress-strain (σ_e-ε_e) curves of AN1173, PA-AN1173, AN1173-AG, and PA-AN1173-AG samples are shown in Fig. 5a. The inset shows other samples subjected to varying annealing temperatures.

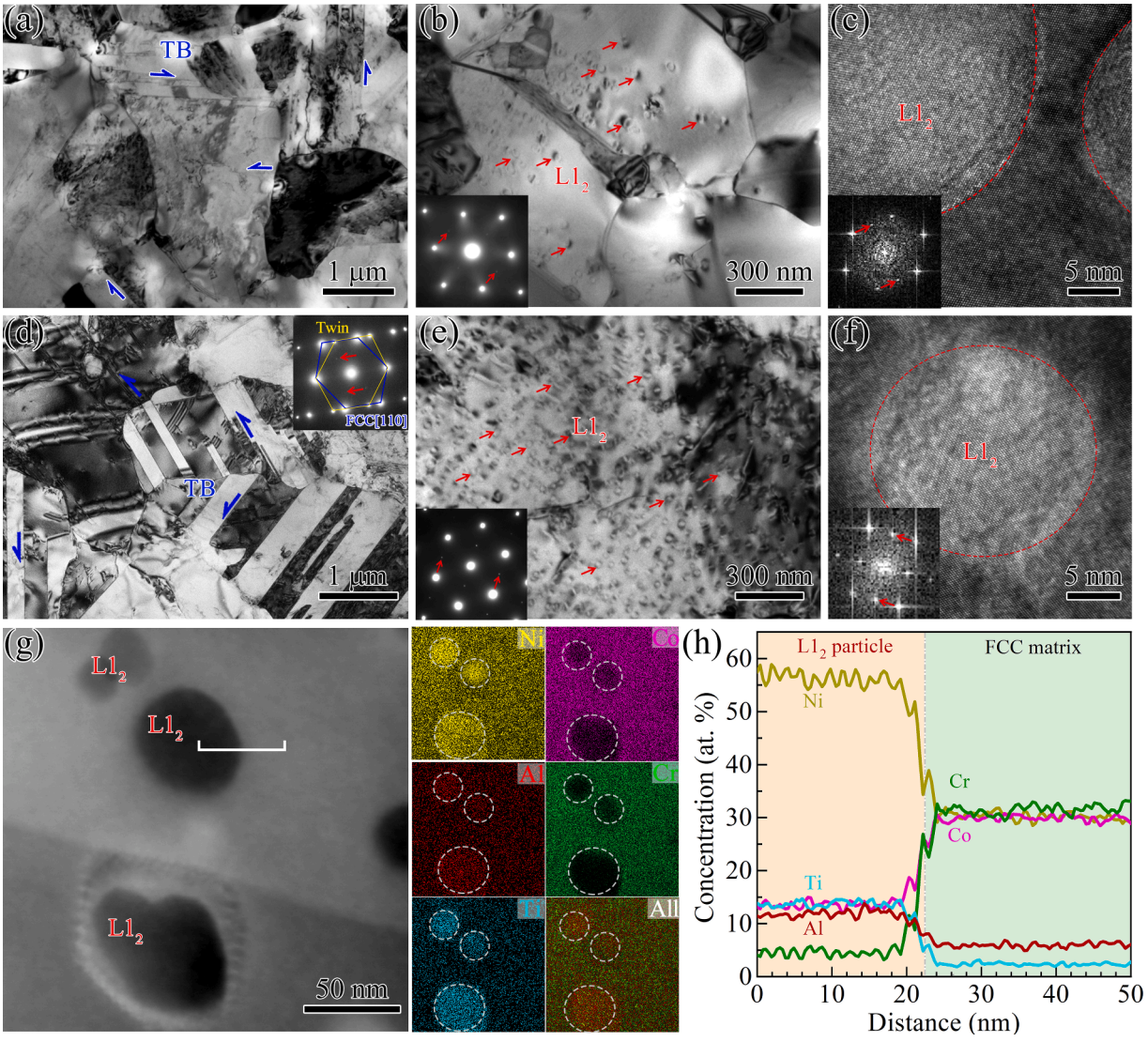

Fig. 3. Characterization of $L1_2$ nanoprecipitates for annealed samples. (a-b) Bright-field TEM images for AN1173. (d-e) Bright-field TEM images for PA-AN1173. HRTEM observations showing coherent interfaces of FCC matrix and $L1_2$ phase for (c) AN1173 and (f) PA-AN1173. (g) EDS mapping for an area with several $L1_2$ nanoprecipitates in AN1173. (h) Element concentrations along the solid line in (g).

It is interesting to note that the additional pre-aging treatment can significantly increase the ductility (uniform elongation, ε_U) while maintaining a similar yield strength (σ_y). In other words, the yield strengths of PA-AN1173 and PA-AN1173-AG (about 1040 MPa and 1420 MPa) are very similar to those of AN1173 and AN1173-AG (about 1100 MPa and 1460 MPa), while the uniform elongations of PA-AN1173 and PA-AN1173-AG (about 26.3 % and 11.2 %) are much higher than that of AN1173 and AN1173-AG (about 16.5 % and 4.5 %).

Stain-hardening rate (θ) and true stress (σ_T) as a function of true strain (ε_T) are plotted in Fig. 5b. It is observed that the pre-aged samples (solid lines) have a more obvious up-turn phenomenon and higher θ, as compared to the samples without pre-aging treatment (dashed lines). The up-turn phenomenon has been widely observed in hetero-structured materials, such as gradient structures (Qin et al., 2022a; Wu et al., 2016), heterogeneous lamella structures (He et al., 2019; Wu et al., 2015), and heterogeneous nanoprecipitated structures (Fan et al., 2020; Qin et al., 2022c). Significantly, the more obvious up-turn phenomenon, the better ductility (Yao et al., 2022; Zhu et al., 2023; Chang et al., 2022; Guan et al., 2021). As reported (Wu et al. 2014), the up-turn phenomenon is due to the more mobile dislocations and extra strain hardening for increasing the material ductility. Thus, the pre-aging treatments can give rise to a more obvious up-turn phenomenon, resulting in better uniform elongation. The tensile properties (σ_y vs. ε_U) for four different heat-treatment procedures are summarized in Fig. 5c. Overall, it can be concluded that additional pre-aging treatment can result in better tensile properties in this MEA.

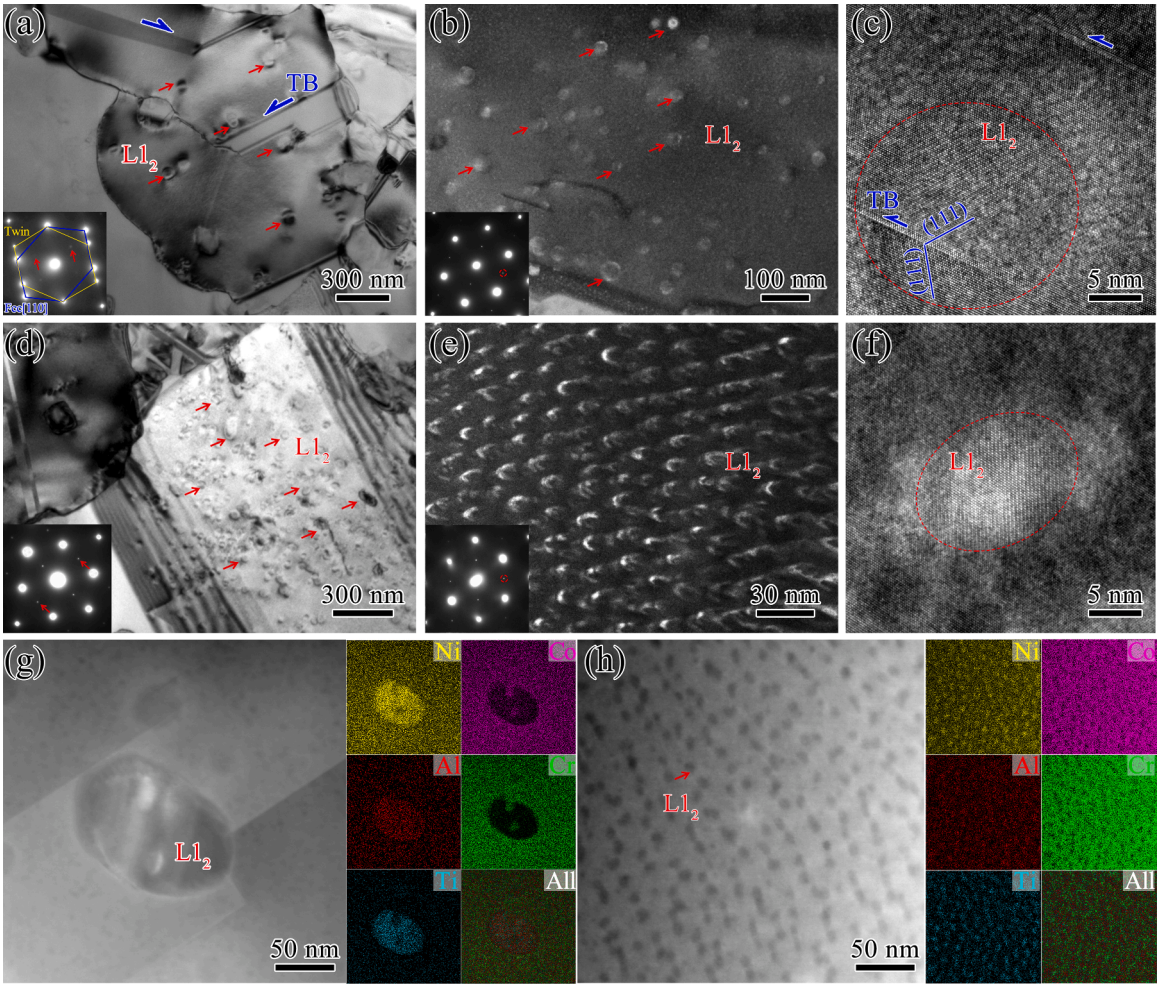

Fig. 4. Characterization of $L1_2$ nanoprecipitates for aged samples. (a) Bright-field TEM image and (b) dark-field TEM image for AN1173-AG. (d) Bright-field TEM image and (e) dark-field TEM image for PA-AN1173-AG. HRTEM observations showing coherent interfaces of FCC matrix and $L1_2$ phase for (c) AN1173-AG and (f) PA-AN1173-AG. EDS mapping for an area with several $L1_2$ nanoprecipitates in (g) AN1173-AG and (h) PA-AN1173-AG.

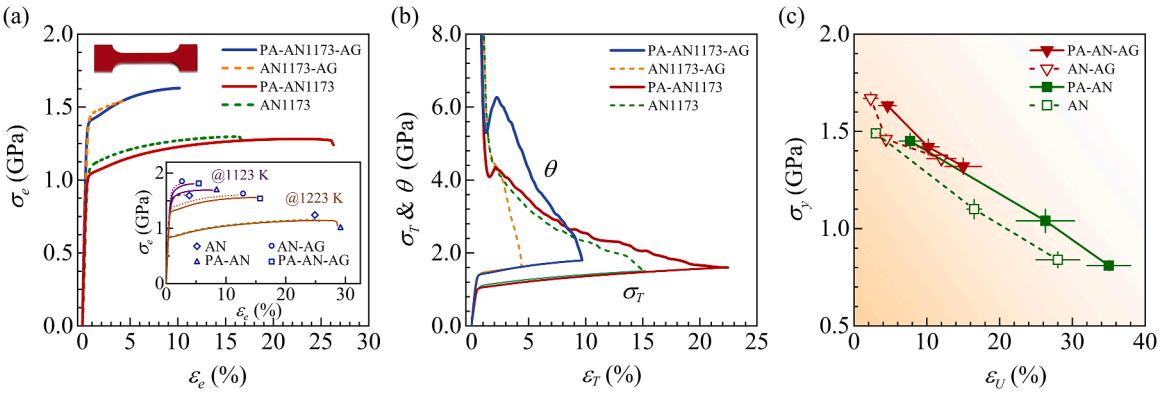

Fig. 5. Mechanical properties and yield strength-ductility balance. (a) Engineering stress-strain (σ_e-ε_e) curves of AN1173, PA-AN1173, AN1173-AG, PA-AN1173-AG. Inset: σ_e-ε_e curves for other samples varying the annealing temperature. (b) Strain hardening rates (θ) and true stress (σ_T) as a function of true strain (ε_T) for AN1173, PA-AN1173, AN1173-AG, PA-AN1173-AG. (c) Yield strength vs. uniform elongation.

3.3. HDI hardening of MEA

In general, hetero-deformation-induced (HDI) hardening plays a crucial role in the ductility of heterogeneous structures (Chou et al., 2022; Yang et al., 2018a). To verify it, the load-unload-reload (LUR) tensile tests were conducted for AN1173, PA-AN1173, AN1173-AG, and PA-AN1173-AG. Fig. 6a shows the true stress-strain curves of the above samples. The close-up view of a mechanical hysteresis loop of PA-AN1173-AG was demonstrated in Fig. 6b. The mechanical hysteresis loop was the characteristic response, indicating the key role of geometrically necessary dislocations (GNDs) in producing the GND-based HDI stress (σ_{HDI}) during plastic deformation (Zhu and Wu, 2023). σ_{HDI} is defined as half of the sum of unloading yield stress (σ_{un}) and reloading yield stress (σ_{re}) (Zhu and Wu, 2023). Accordingly, as shown in Fig. 6c, the σ_{HDI} accounts for more than half of flow stress (σ_f). This suggests that the HDI stress elevates the flow stress by the significant HDI strain hardening effect in the overall deformation process. Of special note are the higher ratios (σ_{HDI}/σ_f) of pre-aged samples than those which were not pre-aged. This also indicated the higher frequency of interactions between GNDs and coherent $L1_2$ nanoprecipitates in pre-aged samples, which will be confirmed by the following experiments.

Strain gradient and GND can be reflected by the kernel average misorientation (KAM) of samples after straining based on the strain gradient theory (Gao et al., 1999; Zhu et al., 2021). KAM mappings and the corresponding mappings of GND density were calculated by EBSD, as shown in Fig. 7. Here, the KAM values above 5° are excluded from the calculation, because these points are assumed to belong to adjacent grains or subgrains. Fig. 7a and b show the GND maps of AN1173-AG and PA-AN1173-AG samples prior to tensile testing, and Fig. 7c and d show the GND maps at the strain of 4.5 %, respectively. After tensile strain (at the strain of 4.5 %), the higher density of GNDs appeared in the vicinity of grain boundaries (GBs) in the AN1173-AG sample (Fig. 7c). In comparison, a more pronounced higher density of GNDs appeared not only around the GBs but also inside the grains in the PA-AN1173-AG sample (Fig. 7d). These differences can be attributed to the high density and random distribution of $L1_2$ nanoprecipitates due to the pre-aging. Then, the statistics distributions of GND density for these two samples are displayed in Fig. 7e-7f. The average GND density increments by 4.5 %-strain were 2.0 and 3.1 $\times$ 10^{14} m^{-2} for the AN1173-AG and PA-AN1173-AG samples, respectively, as shown in Fig. 7g. It is interesting to note that the increment of average GND density for the PA-AN1173-AG sample is much higher than that of the AN1173-AG sample. These results indicated that the pre-aged samples could promote higher-density GNDs and significant HDI hardening for better ductility by the more randomly distributed coherent nanoprecipitates. In addition, grain refinement can be observed in the aged samples after deformation (Fig. 7c and d), due to the high-density deformation twins being promoted during tensile deformation. As reported previously, the corner twins can be formed as a precursor during deformation in CoCrNi-based MEAs with low stacking faults energy, and grain refinement can be induced by further strain (Yang et al., 2018a). The significant refinement of grain also could improve the ductility by increasing the strain hardening during deformation.

3.4. Precipitation hardening of MEA

The XRD patterns for the four samples (AN1173, PA-AN1173, AN1173-AG, PA-AN1173-AG) after tensile deformation are displayed in Fig. 8. The relative volume fractions of the $L1_2$ phase for four samples were estimated to be about 6.5 %, 9.1 %, 13.4 %, and 12.3 %, respectively, which are smaller than those prior to tensile testing. The reduction of volume fraction might be due to the plastic deformation and fragmentation of $L1_2$ nanoprecipitates since $L1_2$ nanoprecipitates can be cut and sheared by dislocations and stack faults (Ming et al., 2018), as revealed by TEM observations.

The deformation mechanism between defects and precipitations was revealed by TEM and HRTEM. Fig. 9 shows the TEM micrographs of AN1173-AG after tensile deformation. The bright-field TEM image (Fig. 9a) shows numerous dislocations, especially around the twin boundaries after tensile deformation. Fig. 9b and c reveal the interactions between defects (dislocations and stacking faults) and coherent $L1_2$ nanoprecipitates. Stacking faults (SFs) inevitably sheared $L1_2$ nanoprecipitates that were spatially distributed in the matrix, as shown in Fig. 9c. Lomer-Cottrell (L-C) locks and 9R structures cut through $L1_2$ nanoprecipitates after tensile

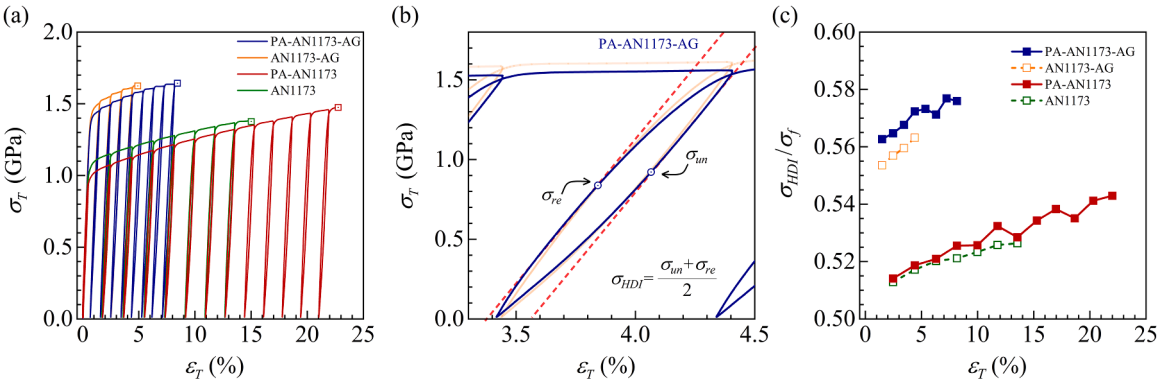

Fig. 6. Hetero-deformation-induced (HDI) hardening. (a) True stress-strain (σ_T-ε_T) curves of load-unload-reload test for AN1173, PA-AN1173, AN1173-AG, PA-AN1173-AG. (b) A mechanical hysteresis loop of PA-AN1173-AG. (c) The ratio of HDI stress (σ_{HDI}) to flow stress (σ_f). .

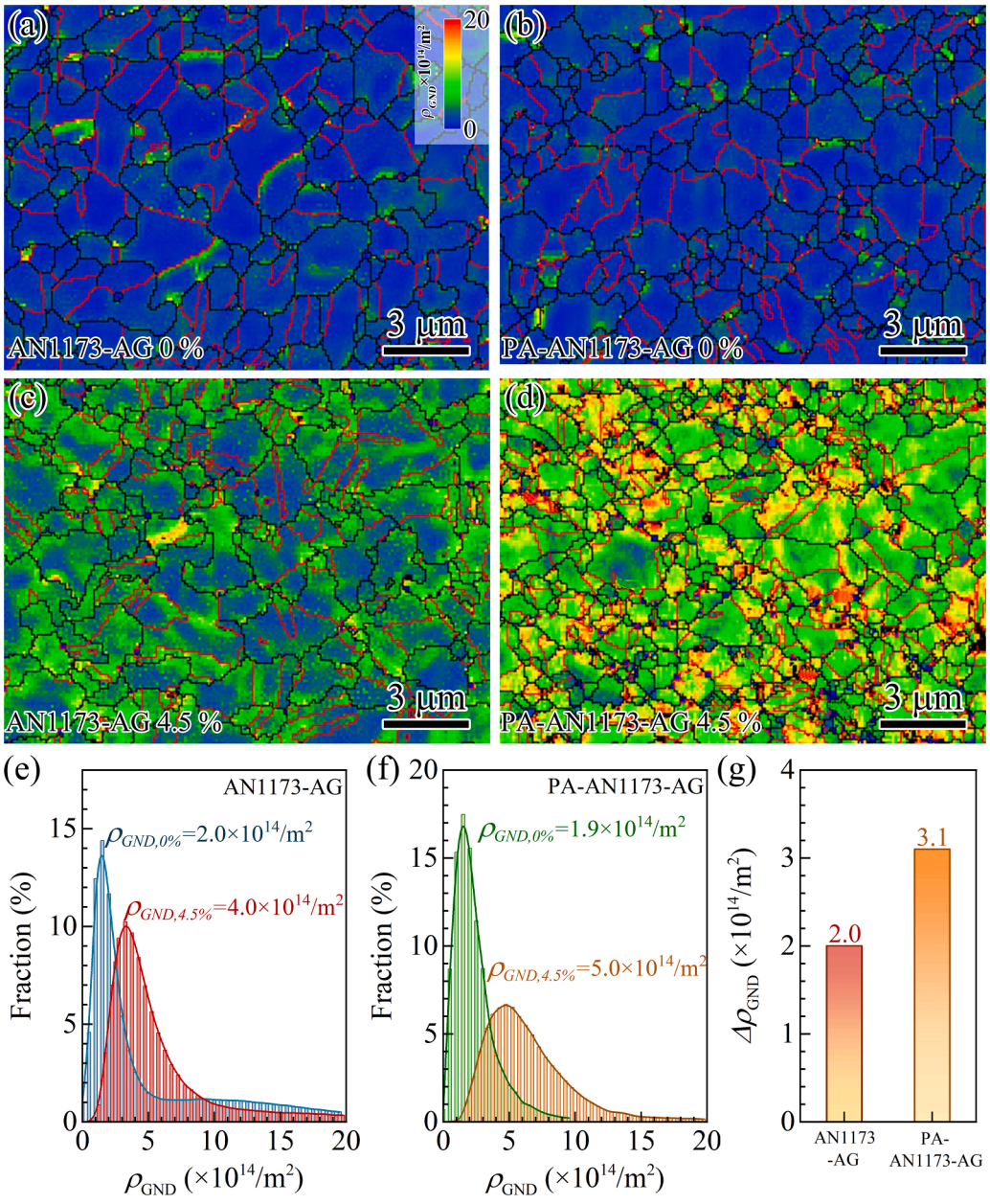

Fig. 7. Evolution of GND density for aged samples at the strain of 0 % and 4.5 %. (a-b) GND density maps for AN1173-AG and PA-AN1173-AG prior to tensile test. (c-d) GND density maps for AN1173-AG and PA-AN1173-AG at the strain of 4.5 %. (e-f) GND density statistics distributions for AN1173-AG and PA-AN1173-AG. (g) The increment of average GND density for the two samples.

deformation, as indicated in Fig. 9d and e. The exact packing sequence of (111) planes for 9R structures is displayed in Fig. 9f by the HRTEM image. Furthermore, it can be seen that the FCC transformed into 9R structures was related to the two parallel arrays of intrinsic stacking faults, i.e., the stacking sequence of (111) planes grind from ABCABCABC to ABCBCACAB. The L-C locks and 9R regions can act as strong barriers to accumulating dislocations around them, significantly enhancing strain hardening (Zhang et al., 2023; Zuo et al., 2019). The precipitate shearing stress (σ_{sh}) associated with dislocation cutting through a precipitate is described as (Ming et al., 2018):

$$\sigma_{sh} = 0.81M\frac{\gamma_{APB}}{2b}\left(\frac{3\pi f}{8}\right)^{1/2}$$

where $M = 3.06$ is the Taylor factor for FCC matrix, γ_{APB}=184 mJ/m^2 is the anti-phase boundary (APB) energy of binary $L1_2$ Ni_3Al

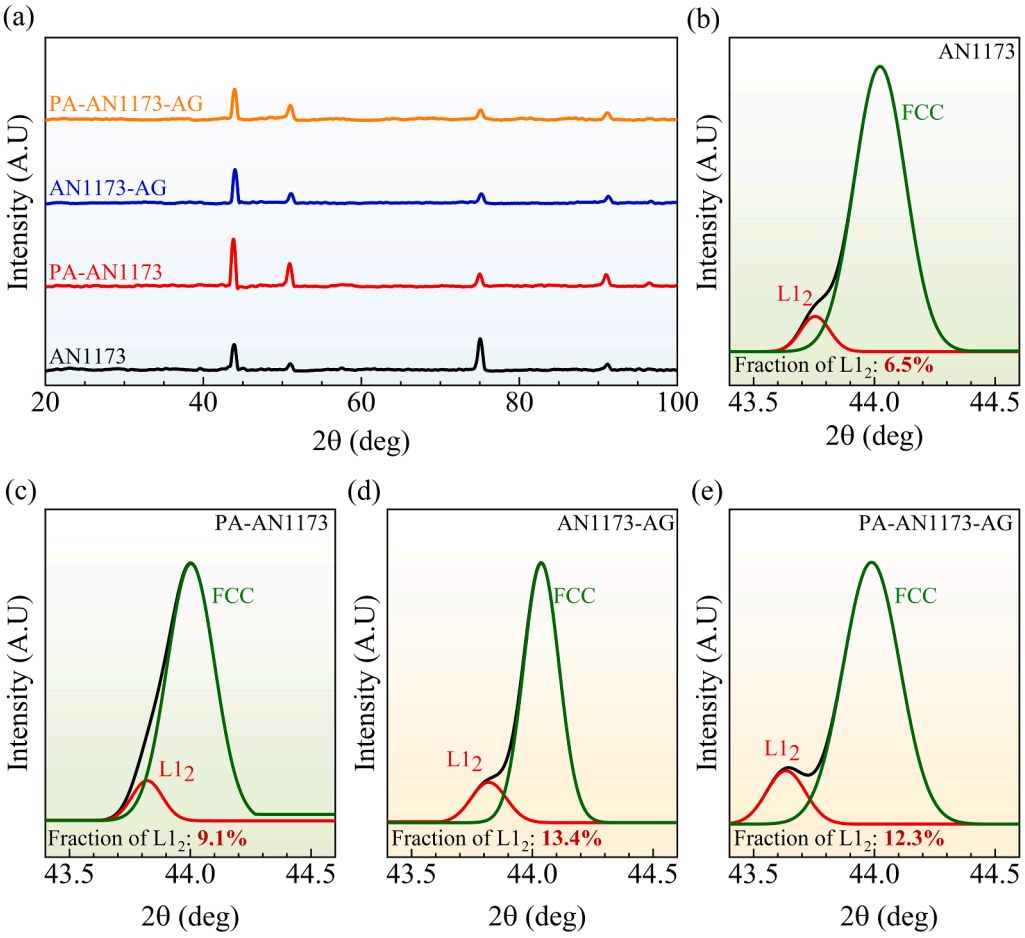

Fig. 8. Phase identification via X-ray diffraction (XRD) analysis after tensile test. (a) XRD patterns for AN1173, PA-AN1173, AN1173-AG, PA-AN1173-AG. The asymmetric (111) diffraction peaks and the deconvoluted symmetric peaks of coherent FCC and $L1_2$ phases for (b) AN1173, (c) PA-AN1173, (d) AN1173-AG, (e) PA-AN1173-AG.

(Ming et al., 2018), f is the volume fraction of precipitates, and b is the Burgers vector (0.262 nm). The volume fractions of $L1_2$ nanoprecipitates are 18.2 % and 10.0 % for AN1173-AG and AN1173, respectively. Accordingly, the σ_{sh} of AN1173-AG is higher by 250 MPa than that of AN1173, accounting for about 70 % of their yield strength increment (360 MPa). Thus, the $L1_2$ nanoprecipitate hardening is the dominant strengthening mechanism for the aged MEA.

TEM observations of PA-AN1173-AG during tensile deformation are shown in Fig. 10. At the strain of 2 %, the beginning of the strain-hardening rate up-turn, only a few SFs and partial dislocations were active at first due to the low stacking fault energy (Fig. 10a-b). Some partial pile-ups were marked by green arrows in Fig. 10b. At the strain of 5 %, deformation twins formed and broadened at approximately the end of the up-turn, as shown in Fig. 10c. At the strain of 10 %, high-density dislocations were observed not only around the TBs and GBs, but also inside the grains interacting with the nanoprecipitates due to increasing strain (Fig. 10d-f), which is consistent with EBSD results (Fig. 7). More randomly distributed $L1_2$ nanoprecipitates with smaller sizes, smaller interspacing, and higher density were sheared by dislocations and SFs, as shown in Fig. 10e. The cutting of precipitates is known to promote planar slip of dislocations, which favors GNDs piling up to produce high HDI stress (Zhu and Wu, 2023). L-C locks and 9R structures are also formed in the PA-AN1173-AG sample at 10 %-strain (Fig. 10g-i). These deformation-induced 9R regions have widths of tens of nanometers (Fig. 10h-i). 9R structures are easily formed in metals and alloys with low stacking fault energy, which could also be formed in metals and alloys with medium/high stacking fault energy under high-strain-rate deformation (Liu et al., 2023b; Zhang et al., 2023, 2022b; Zuo et al., 2019). These kinds of planar defects (such as 9R structures) should be very effective in strengthening/hardening by blocking dislocation slips (Zhang et al., 2023; Zuo et al., 2019). Consequently, more interactions between defects (dislocations, parallel sets of stacking faults, and 9R structures) and coherent $L1_2$ nanoprecipitates can occur in PA-AN1173-AG, as compared to AN1173-AG. These intense interactions should provide significant strain hardening in the pre-aged samples, resulting in better ductility.

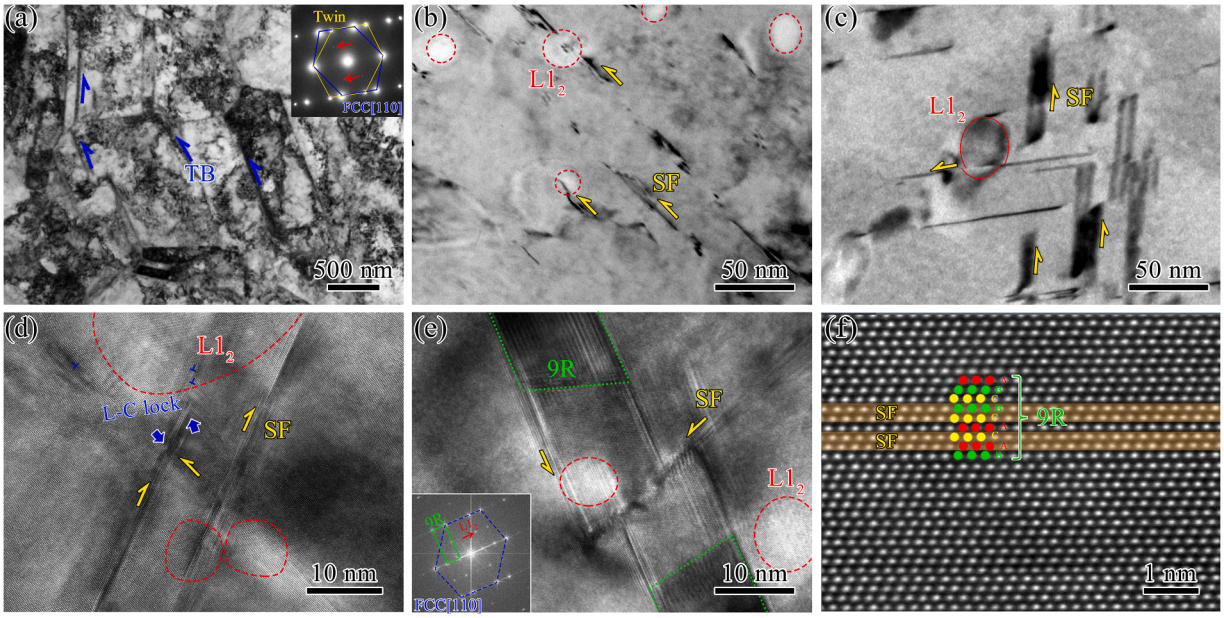

Fig. 9. TEM and HRTEM images after tensile deformation for AN1173-AG. (a-b) Bright-field images showing the $L1_2$ nanoprecipitates and SFs. (c) Shearable $L1_2$ nanoprecipitate. (d) L-C locks. (e) 9R structures and $L1_2$ nanoprecipitates. (f) The packing sequence of 9R structures.

4. Conclusions

Heterogeneous grain structured $(CrCoNi)_{94}Al_4Ti_2$ MEA with coherent $L1_2$ nanoprecipitates was achieved by annealing and aging for different periods. More randomly distributed nanoprecipitates with more uniform size can be obtained by an additional pre-aging treatment. Then, the tensile properties and the corresponding deformation mechanism have been studied, and the key findings are summarized as follows:

(1) Tensile tests reveal a greater increase in uniform elongation without apparently sacrificing strength for the pre-aged MEA. A more obvious up-turn phenomenon on the strain hardening rate curve can be observed for the pre-aged MEA. Thus, a better combination of yield strength and ductility can be achieved by pre-aging.
(2) The $L1_2$ nanoprecipitates can be sheared by dislocations, and the improvement of yield strength is ascribed to the enhanced precipitate shear strength for the aged MEA in comparison to annealed MEA. The cutting of nanoprecipitates can promote planar slip of dislocation, which favors GNDs piling up to produce high HDI stress.
(3) Various defects, including stacking faults, Lomer-Cottrell locks, and 9R structures, were formed during the tensile deformation producing significant strain hardening by blocking and accumulating dislocation.
(4) Higher frequency of interactions between defects and coherent $L1_2$ nanoprecipitates can be found in the pre-aged MEA due to the more randomly distributed $L1_2$ nanoprecipitates, resulting in better ductility. This finding demonstrates a new route to achieving a super strength-ductility combination of single-phase FCC HEAs by nanoscale coherent precipitation strengthening.

CRediT authorship contribution statement

Zihan Zhang: Methodology, Formal analysis, Validation, Investigation. **Yan Ma:** Conceptualization, Visualization, Writing - original draft. **Muxin Yang:** Methodology. **Ping Jiang:** Project administration. **Hangqi Feng:** Investigation. **Yuntian Zhu:** Conceptualization, Funding acquisition, Writing - review & editing. **Xiaolei Wu:** Conceptualization, Funding acquisition, Writing - review & editing. **Fuping Yuan:** Conceptualization, Methodology, Funding acquisition, Writing - review & editing.

Declaration of Competing Interest

The authors declare that they have no known competing financial interests or personal relationships that could have appeared to influence the work reported in this paper.

Data availability

All data generated or analyzed during this study are included in the article and are available from the corresponding authors upon request.

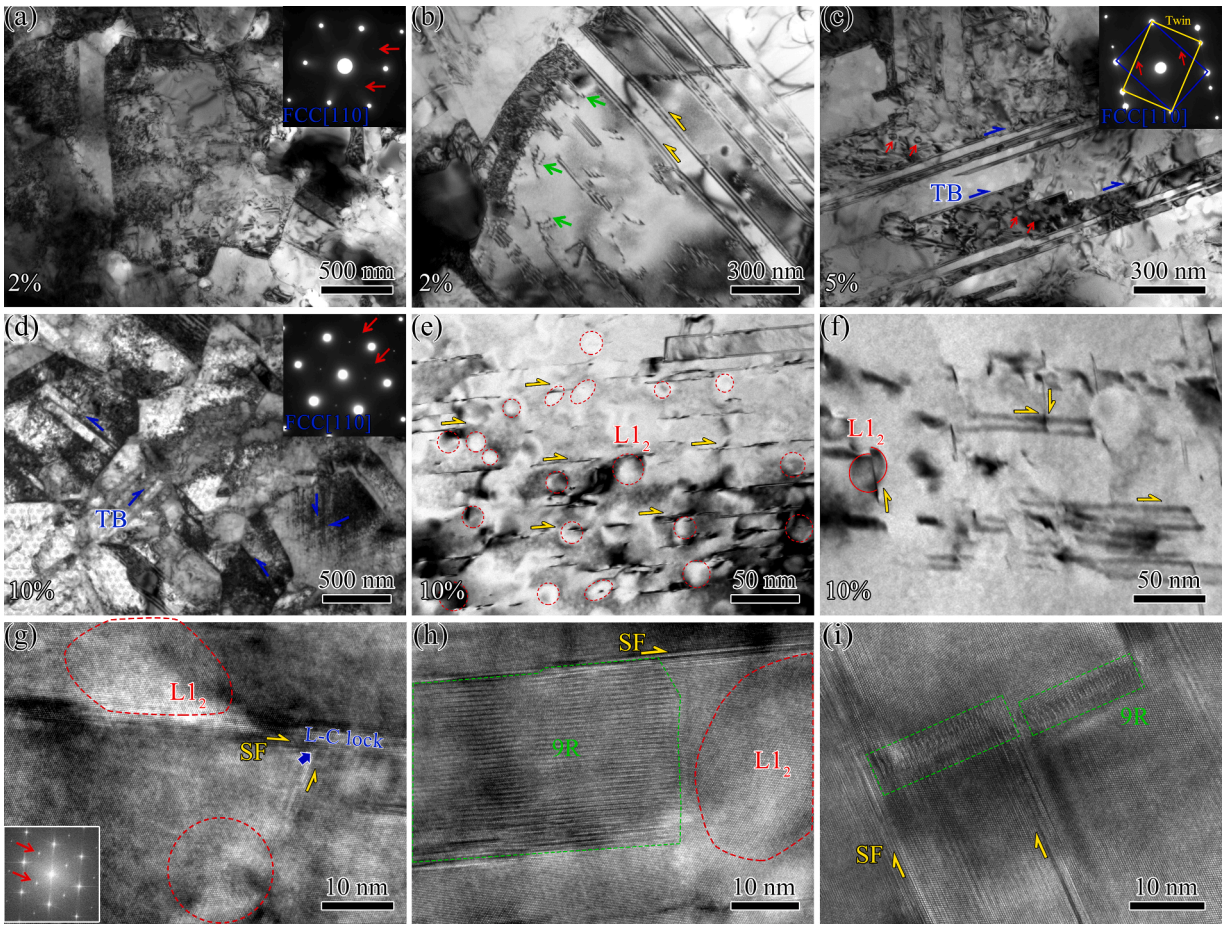

Fig. 10. TEM and HRTEM images during tensile deformation for PA-AN1173-AG. (a-b) Bright-field images showing the dislocations and SFs at 2 %-strain. (c) Bright-field image showing the deformation twins at 5 %-strain. (d-f) Bright-field images showing the deformation twins, $L1_2$ nano-precipitates, and SFs at 10 %-strain. (g-i) HRTEM showing the L-C locks, 9R structures and $L1_2$ nanoprecipitates at 10 %-strain. .

Acknowledgements

This research was supported by the National Natural Science Foundation of China (NSFC) Basic Science Center Program for "Multiscale Problems in Nonlinear Mechanics" [grant number 11988102], the National Key Research & Development Program of China [grant number 2017YFA0204402], the National Natural Science Foundation of China [grant numbers 52192591 and 11790293], and the Hong Kong Research Grants Council [grant GRF 11214121]. Y.Z. and Y.M. thanks Hong Kong Institute for Advanced Study for supporting their work at City University of Hong Kong.

References

An, Z.B., Mao, S.C., Liu, Y.N., Yang, L.Y., Vayyala, A., Wei, X., Liu, C., Shi, C.J., Jin, H.X., Liu, C.X., Zhang, J.X., Zhang, Z., Han, X.D., 2023. Inherent and multiple strain hardening imparting synergistic ultrahigh strength and ductility in a low stacking faulted heterogeneous high-entropy alloy. Acta Mater 243, 14.

Cao, Z.H., Zhai, G.Y., Ma, Y.J., Ding, L.P., Li, P.F., Liu, H.L., Lu, H.M., Cai, Y.P., Wang, G.J., Meng, X.K., 2021. Evolution of interfacial character and its influence on strain hardening in dual-phase high entropy alloys at nanoscale. Int. J. Plast. 145, 103081.

Chang, H., Zhang, T.W., Ma, S.G., Zhao, D., Bai, T.X., Wang, K., Li, Z.Q., Wang, Z.H., 2022. Strengthening and strain hardening mechanisms in precipitation-hardened CrCoNi medium entropy alloys. J. Alloy. Compd. 896, 9.

Chen, H., Chen, Z., Ji, G., Zhong, S.Y., Wang, H.W., Borbely, A., Ke, Y.B., Brechet, Y., 2021a. Experimental and modelling assessment of ductility in a precipitation hardening AlMgScZr alloy. Int. J. Plast. 139, 102971.

Chen, X.F., Wang, Q., Cheng, Z.Y., Zhu, M.L., Zhou, H., Jiang, P., Zhou, L.L., Xue, Q.Q., Yuan, F.P., Zhu, J., Wu, X.L., Ma, E., 2021b. Direct observation of chemical short-range order in a medium-entropy alloy. Nature 592, 712–716.

Cheng, W.Q., Qin, G.H., Yang, M.X., Wang, W., Yuan, F.P., 2022. Excellent tensile properties and deformation mechanisms in a FeCoNi-based medium entropy alloy with dual-heterogeneous structures. J. Appl. Phys. 132, 8.

Chou, T.H., Li, W.P., Chang, H.W., Du, X.H., Chuang, W.S., Yang, T., Zhu, Y.T., Huang, J.C., 2022. Quantitative analysis of hetero-deformation induced strengthening in heterogeneous grain structure. Int. J. Plast. 159, 103482.

Du, X.H., Li, W.P., Chang, H.T., Yang, T., Duan, G.S., Wu, B.L., Huang, J.C., Chen, F.R., Liu, C.T., Chuang, W.S., Lu, Y., Sui, M.L., Huang, E.W., 2020. Dual heterogeneous structures lead to ultrahigh strength and uniform ductility in a Co-Cr-Ni medium-entropy alloy. Nat. Commun. 11, 7.

Fan, L., Yang, T., Zhao, Y.L., Luan, J.H., Zhou, G., Wang, H., Jiao, Z.B., Liu, C.T., 2020. Ultrahigh strength and ductility in newly developed materials with coherent nanolamellar architectures. Nat. Commun. 11 (8).
Fantin, A., Lepore, G.O., Manzoni, A.M., Kasatikov, S., Scherb, T., Huthwelker, T., d'Acapito, F., Schumacher, G., 2020. Short-range chemical order and local lattice distortion in a compositionally complex alloy. Acta Mater 193, 329–337.
Gao, H., Huang, Y., Nix, W.D., Hutchinson, J.W., 1999. Mechanism-based strain gradient plasticity - I. Theory. J. Mech. Phys. Solids 47, 1239–1263.
George, E.P., Raabe, D., Ritchie, R.O., 2019. High-entropy alloys. Nat. Rev. Mater. 4, 515–534.
Gludovatz, B., Hohenwarter, A., Catoor, D., Chang, E.H., George, E.P., Ritchie, R.O., 2014. A fracture-resistant high-entropy alloy for cryogenic applications. Science 345, 1153–1158.
Gludovatz, B., Hohenwarter, A., Thurston, K.V.S., Bei, H.B., Wu, Z.G., George, E.P., Ritchie, R.O., 2016. Exceptional damage-tolerance of a medium-entropy alloy CrCoNi at cryogenic temperatures. Nat. Commun. 7 (8).
Guan, B., Wang, Y.T., Li, J.B., Zhang, Y., Wang, H., Xin, Y.C., 2021. Comprehensive study of strain hardening behavior of CrCoNi medium-entropy alloy. J. Alloy. Compd. 882, 9.
He, J.Y., Wang, H., Huang, H.L., Xu, X.D., Chen, M.W., Wu, Y., Liu, X.J., Nieh, T.G., An, K., Lu, Z.P., 2016. A precipitation-hardened high-entropy alloy with outstanding tensile properties. Acta Mater 102, 187–196.
He, J.Y., Yuan, F.P., Yang, M.X., Jiao, S.H., Wu, X.L., 2019. Superior mechanical properties and deformation mechanisms of heterogeneous laminates under dynamic shear loading. Mater. Sci. Eng. A-Struct. Mater. Prop. Microstruct. Process. 756, 492–501.
Jo, Y.H., Jung, S., Choi, W.M., Sohn, S.S., Kim, H.S., Lee, B.J., Kim, N.J., Lee, S., 2017. Cryogenic strength improvement by utilizing room-temperature deformation twinning in a partially recrystallized VCrMnFeCoNi high-entropy alloy. Nat. Commun. 8, 8.
Jodi, D.E., Park, J., Park, N., 2019. Precipitate behavior in nitrogen-containing CoCrNi medium-entropy alloys. Mater. Charact. 157, 9.
Li, Q.J., Sheng, H., Ma, E., 2019. Strengthening in multi-principal element alloys with local-chemical-order roughened dislocation pathways. Nat. Commun. 10, 11.
Li, Z.M., Pradeep, K.G., Deng, Y., Raabe, D., Tasan, C.C., 2016. Metastable high-entropy dual-phase alloys overcome the strength-ductility trade-off. Nature 534, 227–230.
Liang, Y.J., Wang, L.J., Wen, Y.R., Cheng, B.Y., Wu, Q.L., Cao, T.Q., Xiao, Q., Xue, Y.F., Sha, G., Wang, Y.D., Ren, Y., Li, X.Y., Wang, L., Wang, F.C., Cai, H.N.A., 2018. High-content ductile coherent nanoprecipitates achieve ultrastrong high-entropy alloys. Nat. Commun. 9, 8.
Liu, L.Y., Zhang, Y., Li, J.P., Fan, M.Y., Wang, X.Y., Wu, G.C., Yang, Z.B., Luan, J.H., Jiao, Z.B., Liu, C.T., Liaw, P.K., Zhang, Z.W., 2022. Enhanced strength-ductility synergy via novel bifunctional nano-precipitates in a high-entropy alloy. Int. J. Plast. 153, 15.
Liu, Q.L., Tian, J.Y., Wei, W.T., 2023a. A model for converting thermal analysis to volume fraction of high carbon bearing steels during low-temperature tempering. J. Mater. Sci. Technol. 136, 212–222.
Liu, X.Y., Liu, C.L., Chen, M., Gao, Y.Z., Wei, L.X., Peng, X.H., Zhang, X.F., 2023b. Multi-principal element alloys with High-density nanotwinned 9R phase. Mater. Des. 229, 11.
Ma, E., Wu, X.L., 2019. Tailoring heterogeneities in high-entropy alloys to promote strength-ductility synergy. Nat. Commun. 10, 10.
Ma, Y., Yuan, F.P., Yang, M.X., Jiang, P., Ma, E., Wu, X.L., 2018. Dynamic shear deformation of a CrCoNi medium-entropy alloy with heterogeneous grain structures. Acta Mater 148, 407–418.
Ma, Y., Zhou, L.L., Yang, M.X., Yuan, F.P., Wu, X.L., 2021. Ultra-high tensile strength via precipitates and enhanced martensite transformation in a FeNiAlC alloy. Mater. Sci. Eng. A-Struct. Mater. Prop. Microstruct. Process. 803, 10.
Ming, K.S., Bi, X.F., Wang, J., 2018. Realizing strength-ductility combination of coarse-grained Al0.2Co1.5CrFeNi1.5Ti0.3 alloy via nano-sized, coherent precipitates. Int. J. Plast. 100, 177–191.
Peng, C., Jia, Y.D., Liang, J., Xu, L., Wang, G., Mu, Y.K., Sun, K., Ma, P., Prashanth, K.G., 2023. Electron beam melting of (FeCoNi)86Al7Ti7 high-entropy alloy. J. Alloy. Compd. 960, 11.
Qin, S., Yang, M.X., Jiang, P., Wang, J., Wu, X.L., Zhou, H., Yuan, F.P., 2022a. Designing structures with combined gradients of grain size and precipitation in high entropy alloys for simultaneous improvement of strength and ductility. Acta Mater. 230, 11.
Qin, S., Yang, M.X., Jiang, P., Wang, J., Wu, X.L., Zhou, H., Yuan, F.P., 2023. Superior dynamic shear properties by structures with dual gradients in medium entropy alloys. J. Mater. Sci. Technol. 153, 166–180.
Qin, S., Yang, M.X., Jiang, P., Yuan, F.P., Wu, X.L., 2022b. Excellent tensile properties induced by heterogeneous grain structure and dual nanoprecipitates in high entropy alloys. Mater. Charact. 186, 13.
Qin, S., Yang, M.X., Liu, Y.K., Jiang, P., Fan, J.T., Yuan, F.P., Wu, X.L., 2022c. Superior dynamic shear properties and deformation mechanisms in a high entropy alloy with dual heterogeneous structures. J. Mater. Res. Technol. 19, 3287–3301.
Seol, J.B., Ko, W.S., Sohn, S.S., Na, M.Y., Chang, H.J., Heo, Y.U., Kim, J.G., Sung, H., Li, Z.M., Pereloma, E., Kim, H.S., 2022. Mechanically derived short-range order and its impact on the multi-principal-element alloys. Nat. Commun. 13, 13.
Sohn, S.S., da Silva, A.K., Ikeda, Y., Kormann, F., Lu, W.J., Choi, W.S., Gault, B., Ponge, D., Neugebauer, J., Raabe, D., 2019. Ultrastrong medium-entropy single-phase alloys designed via severe lattice distortion. Adv. Mater. 31, 8.
Song, H.Y., Wang, Y.P., Esling, C., Wang, G.D., Liu, H.T., 2021. The role of grain colony on secondary recrystallization in grain-oriented electrical steel: new insights from an original tracking experiment. Acta Mater. 206, 116611.
Wagner, C., Laplanche, G., 2023. Effects of stacking fault energy and temperature on grain boundary strengthening, intrinsic lattice strength and deformation mechanisms in CrMnFeCoNi high-entropy alloys with different Cr/Ni ratios. Acta Mater. 244, 17.
Wang, J., Jiang, P., Yuan, F.P., Wu, X.L., 2022. Chemical medium-range order in a medium-entropy alloy. Nat. Commun. 13, 6.
Wang, W.Y., Tang, B., Shang, S.L., Wang, J.W., Li, S.L., Wang, Y., Zhu, J., Wei, S.Y., Wang, J., Darling, K.A., Mathaudhu, S.N., Wang, Y.G., Ren, Y., Hui, X.D., Kecskes, L.J., Li, J.S., Liu, Z.K., 2019. Local lattice distortion mediated formation of stacking faults in Mg alloys. Acta Mater. 170, 231–239.
Wu, X.L., Jiang, P., Chen, L., Yuan, F.P., Zhu, Y.T.T., 2014. Extraordinary strain hardening by gradient structure. Proc. Natl. Acad. Sci. USA 111, 7197–7201.
Wu, X.L., Yang, M.X., Yuan, F.P., Chen, L., Zhu, Y.T., 2016. Combining gradient structure and TRIP effect to produce austenite stainless steel with high strength and ductility. Acta Mater. 112, 337–346.
Wu, X.L., Yang, M.X., Yuan, F.P., Wu, G.L., Wei, Y.J., Huang, X.X., Zhu, Y.T., 2015. Heterogeneous lamella structure unites ultrafine-grain strength with coarse-grain ductility. Proc. Natl. Acad. Sci. USA 112, 14501–14505.
Xu, L., Jia, Y.D., Wang, Z.H., Wu, S.W., Jia, Y.F., Geng, C., Peng, J.C., Tan, X.H., Wang, G., 2023. Dual precipitate simultaneous enhancement of tensile and fatigue strength in (FeCoNi)86Al7Ti7 high-entropy alloy fabricated using selective laser melting. J. Mater. Sci. Technol. 148, 90–104.
Xu, S.S., Zhao, Y., Chen, D., Sun, L.W., Chen, L., Tong, X., Liu, C.T., Zhang, Z.W., 2019. Nanoscale precipitation and its influence on strengthening mechanisms in an ultra-high strength low-carbon steel. Int. J. Plast. 113, 99–110.
Yang, M.X., Yan, D.S., Yuan, F.P., Jiang, P., Ma, E., Wu, X.L., 2018a. Dynamically reinforced heterogeneous grain structure prolongs ductility in a medium-entropy alloy with gigapascal yield strength. Proc. Natl. Acad. Sci. USA 115, 7224–7229.
Yang, T., Zhao, Y.L., Luan, J.H., Han, B., Wei, J., Kai, J.J., Liu, C.T., 2019. Nanoparticles-strengthened high-entropy alloys for cryogenic applications showing an exceptional strength-ductility synergy. Scr. Mater. 164, 30–35.
Yang, T., Zhao, Y.L., Tong, Y., Jiao, Z.B., Wei, J., Cai, J.X., Han, X.D., Chen, D., Hu, A., Kai, J.J., Lu, K., Liu, Y., Liu, C.T., 2018b. Multicomponent intermetallic nanoparticles and superb mechanical behaviors of complex alloys. Science 362, 933–937.
Yang, Y., Chen, T.Y., Tan, L.Z., Poplawsky, J.D., An, K., Wang, Y.L., Samolyuk, G.D., Littrell, K., Lupini, A.R., Borisevich, A., George, E.P., 2021. Bifunctional nanoprecipitates strengthen and ductilize a medium-entropy alloy. Nature 595, 245–249.
Yao, N., Lu, T.W., Feng, K., Sun, B.H., Wang, R.Z., Wang, J., Xie, Y., Zhao, P.C., Han, B.L., Zhang, X.C., Tu, S.T., 2022. Ultrastrong and ductile additively manufactured precipitation-hardening medium-entropy alloy at ambient and cryogenic temperatures. Acta Mater. 236, 14.
Yeh, J.W., Chen, S.K., Lin, S.J., Gan, J.Y., Chin, T.S., Shun, T.T., Tsau, C.H., Chang, S.Y., 2004. Nanostructured high-entropy alloys with multiple principal elements: novel alloy design concepts and outcomes. Adv. Eng. Mater. 6, 299–303.

Zhang, H., Wang, W.R., Yuan, L.H., Wei, Z.L., Zhang, H., Zhang, W.F., 2022a. Quantitative phase analysis of Ti-3Al-5Mo-4.5V dual phase titanium alloy by XRD whole pattern fitting method. Mater. Charact. 187, 10.
Zhang, J.F., Zhou, D.S., Pang, X.Y., Zhang, B.W., Li, Y., Sun, B.H., Valiev, R.Z., Zhang, D.L., 2023. Deformation-induced concurrent formation of 9R phase and twins in a nanograined aluminum alloy. Acta Mater. 244, 12.
Zhang, R.P., Zhao, S.T., Ding, J., Chong, Y., Jia, T., Ophus, C., Asta, M., Ritchie, R.O., Minor, A.M., 2020. Short-range order and its impact on the CrCoNi medium-entropy alloy. Nature 581, 283–287.
Zhang, Y.D., Li, G.P., Yuan, F.S., Han, F.Z., Ali, M., Guo, W.B., Ren, J., 2022b. Atomic scale observation of FCC twin, FCC ->9R and 9R ->12R' transformations in cold-rolled Hafnium. Scr. Mater. 207, 4.
Zhang, Z.H., Jiang, P., Yuan, F.P., Wu, X.L., 2022c. Enhanced tensile properties by heterogeneous grain structures and coherent precipitates in a CoCrNi-based medium entropy alloy. Mater. Sci. Eng. A-Struct. Mater. Prop. Microstruct. Process. 832, 11.
Zhang, Z.H., Ma, Y., Qin, S., Wang, J., Yang, M.X., Jiang, P., Wu, X.L., Yuan, F.P., 2022d. Unusual phase transformation and novel hardening mechanisms upon impact loading in a medium entropy alloy with dual heterogeneous structure. Intermetallics 151, 11.
Zhang, Z.H., Wang, W., Qin, S., Yang, M.X., Wang, J., Jiang, P., Yuan, F.P., Wu, X.L., 2022e. Dual heterogeneous structured medium-entropy alloys showing a superior strength-ductility synergy at cryogenic temperature. J. Mater. Res. Technol. 17, 3262–3276.
Zhao, Y., Xiao, W., Zhao, Z., Li, Q., Cui, J., Luan, J., Liu, C., Liaw, P.K., Yang, T., 2023. A Co-rich chemically complex intermetallic alloy with extraordinary strength-ductility synergy. Scr. Mater. 229, 6.
Zhou, L.L., Wang, Q., Wang, J., Chen, X.F., Jiang, P., Zhou, H., Yuan, F.P., Wu, X.L., Cheng, Z.Y., Ma, E., 2022. Atomic-scale evidence of chemical short-range order in CrCoNi medium-entropy alloy. Acta Mater. 224, 11.
Zhu, J.Q., Sun, L.G., Li, D.F., Zhu, L.L., He, X.Q., 2023. Compositional undulation induced strain hardening and delocalization in multi-principal element alloys. Int. J. Mech. Sci. 241, 12.
Zhu, Y.T., Ameyama, K., Anderson, P.M., Beyerlein, I.J., Gao, H.J., Kim, H.S., Lavernia, E., Mathaudhu, S., Mughrabi, H., Ritchie, R.O., Tsuji, N., Zhang, X.Y., Wu, X.L., 2021. Heterostructured materials: superior properties from hetero-zone interaction. Mater. Res. Lett. 9, 1–31.
Zhu, Y.T., Liao, X.Z., 2004. Nanostructured metals - Retaining ductility. Nat. Mater. 3, 351–352.
Zhu, Y.T., Wu, X.L., 2023. Heterostructured materials. Prog. Mater. Sci. 131, 55.
Zuo, J.D., He, C., Cheng, M., Wu, K., Wang, Y.Q., Zhang, J.Y., Liu, G., Sun, J., 2019. Heterophase interface-mediated formation of nanotwins and 9R phase in aluminum: underlying mechanisms and strengthening effect. Acta Mater. 174, 279–288.